CrossMark

J͞M PAPERS

Intrinsic and apparent slip at gas-enriched liquid–liquid interfaces: a molecular dynamics study

Emanuele Telari[1], Antonio Tinti[1] and Alberto Giacomello[1],†

[1]Dipartimento di Ingegneria Meccanica e Aerospaziale, Sapienza Università di Roma, Via Eudossiana 18, 00184 Rome, Italy

In this paper, slip at liquid–liquid interfaces is studied focusing on the ubiquitous case in which a third species (e.g. a gas) is present. Non-equilibrium molecular dynamics simulations demonstrate that the contaminant species accumulate at the liquid–liquid interface, enriching it and affecting momentum transfer in a non-trivial fashion. The Navier boundary condition is seen to apply at this interface, accounting for slip between the liquids. Opposite trends are observed for soluble and poorly soluble species, with the slip length decreasing with concentration in the first case and significantly increasing in the latter. Two regimes are found, one in which the liquid–liquid interface is altered by the third species but changes in slip length remain limited to molecular sizes (intrinsic slip). In the second regime, further accumulation of non-soluble gas at the interface gives rise to a gaseous layer replacing the liquid–liquid interface; in this case, the apparent slip lengths are one order of magnitude larger and grow linearly with the layer width as captured quantitatively by a simple three-fluids model. Overall, results show that the presence of a third species considerably enriches the slip phenomenology both calling for new experiments and opening the door to novel strategies to control liquid–liquid slip, e.g. in liquid infused surfaces.

Key words: non-continuum effects, multiphase flow, molecular dynamics

1. Introduction

Although already hypothesized by Navier (1823), slip at fluid boundaries has become the object of intense research only with the rapid growth of microfluidics and nanofluidics

† Email address for correspondence: alberto.giacomello@uniroma1.it

(Lauga, Brenner & Stone 2007). At such scales, the importance of interface phenomena is magnified to such an extent that fluid flow may be altered (Barrat & Chiaruttini 2003; Bocquet & Charlaix 2009) or even dominated (Secchi *et al.* 2016) by slip at the boundaries. Because of its immediate technological relevance, the case of liquid slip at solid walls has been studied in great detail (Lauga *et al.* 2007; Rothstein 2010). By contrast, the present contribution focuses on the less investigated case of liquid–liquid slip, which is of emerging importance due to the popularization of technologies based on liquid–liquid interfaces such as liquid-infused surfaces (LIS).

In recent years, it has been recognized that distinct mechanisms may give rise to slip at (liquid–solid) boundaries (Cottin-Bizonne *et al.* 2005; Lauga *et al.* 2007; Vinogradova & Belyaev 2011): intrinsic slip, originating in the molecular interactions at the interface between two pure phases; and apparent slip, arising from diverse phenomena at heterogeneous interfaces, e.g. gaseous bubbles entrapped at a superhydrophobic wall. While intrinsic slip, measured in terms of slip length, is generally limited to molecular sizes (Chinappi & Casciola 2010), the magnitude of apparent slip lengths at rough solid walls can be of the order of micrometres (Choi & Kim 2006; Rothstein 2010). Such large slip lengths are directly relevant to manipulate the flow in microfluidic applications but are also promising in reducing drag in larger-scale applications, including turbulent flows (Daniello, Waterhouse & Rothstein 2009; Rothstein 2010; Costantini, Mollicone & Battista 2018).

Grafting with polymer brushes has also been explored as a means of inducing hydrodynamic slip at a solid–liquid interface (Brochard & De Gennes 1992; Charrault *et al.* 2016). A more common strategy to achieve large apparent slip is to promote the formation of wall-attached gaseous pockets by using rough, hydrophobic surfaces; under favourable conditions, such properties give rise to the 'suspended' superhydrophobic state, which in turn induces large apparent slip lengths (Cottin-Bizonne *et al.* 2003; Ybert *et al.* 2007; Rothstein 2010; Gentili *et al.* 2013, 2014). However, a common problem of the superhydrophobic state is related to its fragility (Giacomello *et al.* 2016, 2019), i.e. the fact that pressure variations may overcome the capillary forces sustaining the liquid–gas interface leading to the fully wet Wenzel state. In such a state, slip vanishes and drag typically increases as compared with a smooth surface (Maali *et al.* 2012).

Recently, in order to overcome the limitations of superhydrophobic surfaces, LIS have been devised (Lafuma & Quéré 2011; Wong *et al.* 2011; Smith *et al.* 2013), in which the rough solid is covered by a layer of a second, immiscible liquid, usually oil. Due to its incompressibility, this liquid layer does not suffer from the fragility of the superhydrophobic state, while maintaining many of its favourable properties (Mistura & Pierno 2017; Semprebon, McHale & Kusumaatmaja 2017). For instance, recent works have predicted (Asmolov, Nizkaya & Vinogradova 2018) or measured large apparent slip lengths at LIS (Solomon, Khalil & Varanasi 2014; Scarratt, Zhu & Neto 2020) and even potential for turbulent drag reduction (Fu *et al.* 2017; Cartagena *et al.* 2018). In particular, some of the recently reported values of the slip length at oil-infused surfaces are surprisingly large, up to 250 nm (Scarratt *et al.* 2020), which urgently calls for a thorough investigation of its microscopic origin. Is it due to intrinsic slip at the liquid–liquid interface? What experimental parameters affect it?

Molecular dynamics simulations seem to suggest that there is an intrinsic slip connected with the interface of two simple liquids, but its magnitude is of atomic size (Padilla, Toxvaerd & Stecki 1995; Koplik & Banavar 1998, 2006; Buhn, Bopp & Hampe 2004; Galliero 2010). A similar scenario also applies to polymers and chain-like molecules (Goveas & Fredrickson 1998; Barsky & Robbins 2001) often employed in LIS.

Several extrinsic factors may influence slip at a liquid–liquid interface; for instance, the presence of surfactants may decrease or even suppress slip (Hu, Zhang & Wang (2010) – see also Bolognesi, Cottin-Bizonne & Pirat (2014) and Peaudecerf *et al.* (2017) for the case of liquid–gas interfaces). On the other hand, the presence of a gas layer may enhance slip of liquid–liquid interfaces: in Hemeda & Tafreshi (2016), a special LIS supporting three superimposed fluid layers has been proposed – water, oil and air – which decreases drag as compared with standard LIS. At the nanoscale, it has been hypothesized that hydrophobic nanoparticles may act as ball bearings separating two liquid interfaces and lead to giant slip (Ehlinger, Joly & Pierre-Louis 2013); whereas there might be practical difficulties in preventing the hydrophobic aggregation of such nanobearings, the idea of interposing a nanoscale gaseous layer between two liquids is fascinating and will be explored in the present work.

Recent research has focused on the effect of dissolved gases on various aspects of fluid behaviour at the nanoscale. In particular, dissolved gases have been shown to have a significant effect on the phase stability of liquid water confined in nanopores (Tinti *et al.* 2017; Tinti, Giacomello & Casciola 2018; Camisasca, Tinti & Giacomello 2020) and in the formation of surface nanobubbles (Tortora *et al.* 2020). Importantly, in both cases it was shown that poorly soluble species tend to accumulate at interfaces. In the same spirit, in the present work we investigate whether dissolved third species selectively accumulate at a liquid–liquid interface and their potential for controlling and tuning liquid–liquid slip.

It is clear from the previous discussion that apparent slip, both at superhydrophobic surfaces and at LIS, is rooted in the complex flow phenomena at a composite liquid–solid–fluid interface. In particular, the flow that is established depends on the boundary conditions, which are in turn determined by the intrinsic slip at liquid–solid, liquid–liquid or liquid–gas interfaces. Here, we investigate via molecular dynamics simulations the microscopic mechanism(s) of liquid–liquid slip, in particular in the poorly explored case in which a third species is present. The slip properties are expected to vary depending on where and how such species accumulate, e.g. between the two liquids. With this in mind, we simulate slip in the presence of dissolved gases with different solubilities. Anticipating our results, we find that poorly soluble species indeed accumulate at the interface and can increase more than 10 times the liquid–liquid slip length, depending on their concentration. On the other hand, more soluble species act in the opposite direction of decreasing the liquid–liquid slip, halving it at the highest explored concentrations.

1.1. *Slip at an idealized liquid-infused surface*

Several slip phenomena may occur at LIS, which are generally difficult to disentangle in experiments. Here we attempt to review them and to rationalize one of them, i.e. slip at the liquid–liquid interface. In figure 1 we present a simplified scheme of the main mechanisms that lead to slip, and thus drag reduction, at an LIS in the presence of a laminar flow.

The thin lubricant layer, generally an oil, which covers the solid surface is typically characterized by a lower viscosity than the working fluid, generally water, leading to a strong velocity gradient very close to the solid boundary. Observing the LIS at some distance, it is possible to account for the effect of such thin lubricant layer with an effective slip length. This amounts to approximating the location of the solid boundary with the oil–water interface, which is often a safe assumption since h_o is typically very small (Scarratt *et al.* (2020); consider $0 < h_o < 500$ nm, where h_o is the thickness of the oil layer). It is easy to show (Ybert *et al.* 2007) that the apparent slip length introduced by
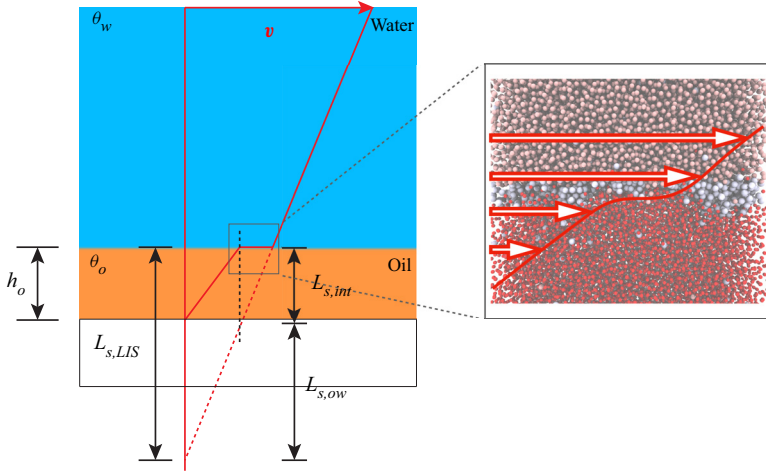
Figure 1. Schematic view of the flow in the vicinity of an LIS. Here $L_{s,ow}$ represents the effective slip length measured at the surface due to the presence of a slab of lubricant; $L_{s,int}$ measures the contribution of the slip at the interface between the working fluid (typically water, in blue) and the lubricant (typically oil, in orange) to the total effective slip length at the LIS, $L_{s,LIS}$. The magnification shows the velocity profile at the liquid–liquid interface studied in the present work.

the said thin lubricant layer is given by (see also the supplementary material available at https://doi.org/10.1017/jfm.2022.162)

$$L_{s,ow} = \frac{\mu_w}{\mu_o} h_o, \tag{1.1}$$

where $\mu_{w/o}$ are the dynamic viscosities of water and oil, respectively. Actual values of the viscosity ratio $\gamma_{ow} \equiv \mu_w/\mu_o$ may be of the order of some units; Scarratt *et al.* (2020) use $\gamma_{ow} \approx 4$. According to (1.1), slip due to the oil layer may account for a slip length of up to hundreds of nanometres, depending on the lubricant's nature and thickness.

The second contribution $L_{s,int}$ to the overall slip length comes from the liquid–liquid interface itself, see figure 1 and is the object of this work. Before discussing its origin, it is important to remark that the two contributions to slip at an LIS simply sum, as can be seen by considering a two-phase Couette flow with a Navier condition at the liquid–liquid interface (more details are presented in the supplementary material):

$$L_{s,LIS} = L_{s,ow} + L_{s,int}. \tag{1.2}$$

The slip mechanism ($L_{s,int}$) at the liquid–liquid interface is much less studied than the one originating from the lower viscosity of the interposed oil layer ($L_{s,ow}$) as it is rooted in the molecular interactions at the interface. Recently, the presence of liquid–liquid slip has been invoked to explain unexpected slip measurements at LIS (Scarratt *et al.* 2020). Galliero (2010) studied using molecular dynamics two pure liquids in a shear flow, discussing the dependence of $L_{s,int}$ on the miscibility of the two liquids. Results showed that $L_{s,int}$ is maximum for poorly miscible liquids, due to the depletion in density occurring at the interface. However, the reported absolute values are of molecular size (<1 nm) and account for an intrinsic slip at liquid–liquid interfaces.

In order to clarify whether $L_{s,int}$ can be magnified in some conditions and thus give a measurable contribution to the overall slip at LIS, we consider here a liquid–liquid interface with gas dissolved in the liquids – with the understanding that this third
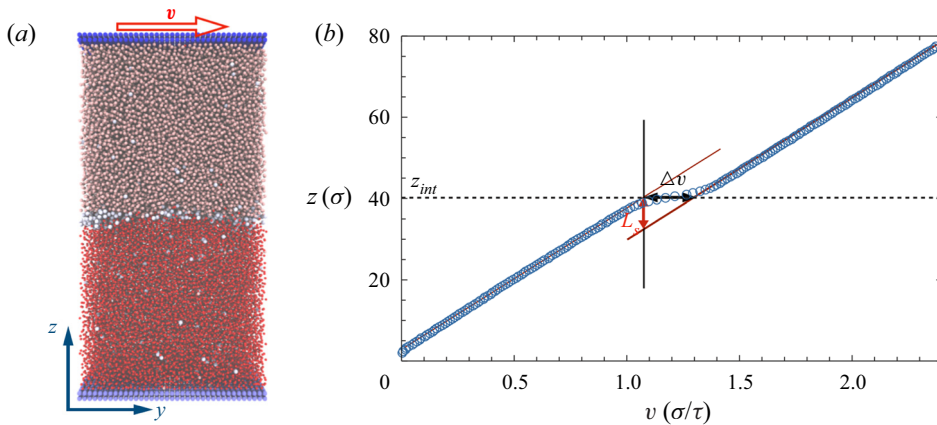
938 A35-4

Figure 2. (*a*) Snapshot of the system: red particles denote liquid 1; pink particles liquid 2; and white particles the third species. The direction orthogonal to the interface plane is the z-axis and the direction going out of the page is the x-axis. The white arrow represents the shear applied to the upper wall in the y direction. (*b*)Average velocity profile (blue, dotted) along the z direction; the interface position is denoted by a dashed line. The velocity jump (Δv) and the slip length (L_s) are also indicated.

species can significantly alter interfacial properties. Dissolved gases are ubiquitous in actual experiments, which are performed in open air (drops at LIS) or in a closed microfluidics environment. Without loss of generality, we characterize the interfacial slip of a well-studied interface, that between two immiscible symmetric liquids, in the presence of an increasing content of gases with different solubilities. We found that interfacial slip can be either of molecular origin (intrinsic slip) or apparent in nature, stemming from the formation of a thin gas layer separating the two liquids. The calculated slip lengths were found to be up to one order of magnitude larger than what is expected for two pure liquids.

The paper is organized as follows. In § 2, the system is introduced and the gas solubilities are characterized – simulations and postprocessing details are given. The reader who is not interested in technical details can jump to § 3, where the results are discussed, including slip lengths as a function of gas content, § 3.1 and the identification of two slip mechanisms: the enrichment of gas of the liquid–liquid interface, § 3.2; and the formation of a gas layer interposed between the two liquids, § 3.3. Section 4 is left for conclusions.

2. Methods

2.1. *The system*

The present work reports the results of non-equilibrium molecular dynamics simulations of a multiphase shear flow (figure 2). The starting point for our investigation is a system composed of two atomic species with symmetric interactions constituting two immiscible liquid phases. Periodic boundary conditions are applied in the directions parallel to the liquid–liquid interface, while rigid atomic walls enclose the system in the third direction. Atoms of a third species were added in increasing amounts to the system in order to investigate their effect on slip properties. Results are reported for different concentrations of this third species and for various interactions strengths with the liquids.

Molecular dynamics simulations were performed using the 'large-scale atomic/molecular massively parallel simulator' (LAMMPS) software (Plimpton 1995). Shearing is obtained by displacing at constant velocity one of the rigid atomic walls that delimit the two liquids,

while the remaining wall is constrained to remain still. Thermostatting of the fluid particles is obtained by using a Nosé–Hoover chain thermostat (Martyna, Klein & Tuckerman 1992) with $N_{chain} = 4$ and a dampening parameter of 100 integration time steps, where the time step adopted is $\Delta t = 0.003\tau$, with $\tau = \sigma(m/\varepsilon)^{1/2}$, where the parameter σ defines the typical size of the particle and ε the energy scale of the interaction. As customary for simulations of shear flows (Todd & Daivis 2017), the thermostat acts only on the degrees of freedom that are orthogonal to the shearing direction. Pressure is controlled by applying a constant force on the moving wall in the direction orthogonal to the liquid–liquid interface. This mechanical barostat is a variation on similar schemes in widespread usage (see, e.g. Chinappi & Casciola 2010) and it allows for an accurate control of the hydrostatic pressure. Further simulation details are presented in the supplementary materials. In particular, we checked that the results were consistent with those obtained with different thermostats and that the system was in the linear response regime.

Interatomic interactions between atoms i and j are described by truncated and shifted Lennard–Jones (LJ) potentials U_{ij}^{LJ}, as follows:

$$
U_{ij}^{LJ} = \begin{cases} 4\varepsilon_{\alpha\beta} \left[\left(\dfrac{\sigma_{\alpha\beta}}{r_{ij}} \right)^{12} - \left(\dfrac{\sigma_{\alpha\beta}}{r_{ij}} \right)^{6} \right] + |U_{LJ}(r_c)| & \text{if } r_{ij} \leqslant r_c \\ 0 & \text{if } r_{ij} > r_c, \end{cases} \tag{2.1}
$$

where indices i and j run over all the atoms and α and β represent the types of atoms i and j, respectively. The total potential energy U can be computed by summing U_{ij}^{LJ} over all pairs $i,j > i$. A cutoff radius $r_c = 3.5\sigma$ was used, matching that of Galliero (2010). Two liquid species were simulated, each defined by LJ parameters $\sigma_{11} = \sigma_{22} = \sigma$, $\varepsilon_{11} = \varepsilon_{22} = \varepsilon$ and with masses $m_1 = m_2 = 1$. The interactions between the two liquids were modulated by multiplying the energy parameter of the liquid–liquid interactions, ε_{12}, by a coefficient $k_{liq} = 0.25$, such that $\varepsilon_{12} = k_{liq}\varepsilon$; this choice of values is used to render two immiscible liquid phases (Galliero 2010), each occupying one half of the system (figure 2).

A total of 46 398 atoms were used for the entire initial system, 2812 of which constitute the two rigid walls and 21 793 for each liquid phase. The system was equilibrated in a box of dimensions $L_x = 20\sigma$, $L_y = 40\sigma$ and average height $L_z = 77.31\sigma$, at the reduced temperature $k_B T/\varepsilon = 1$, with k_B the Boltzmann constant and T the temperature, and keeping the normal pressure, in the z direction, constant at $P_z = 0.4\varepsilon/\sigma^3$, which is held constant also during the shearing of the system. Shearing was obtained by imposing the value $|v| = 2.4\sigma/\tau$, for the streamwise velocity of the upper wall, as illustrated in figure 2.

After an initial equilibration run we introduced different numbers of atoms N_{th} of a third species. The interactions we considered between the liquids and the third species were symmetric and modulated by multiplying the liquid energy parameter by a constant k_{gas}, such that $\varepsilon_{13} = \varepsilon_{23} = k_{gas}\varepsilon$, while the size parameter was kept constant and equal to unity, $\sigma_{13} = \sigma_{23} = \sigma$. Four different values of k_{gas} were considered: 0.125, 0.25, 0.5 and 1.0. The factor multiplying the energy parameter, k_{gas}, made the interactions weaker than or equal to the liquid–liquid ones, thus changing the solubility of the inserted atoms, as characterized below. A broad range of content of the third species was considered, ranging from a minimum of 20 atoms to a maximum of 3600 atoms, corresponding to concentrations going from 0.0004 wt% to 0.0826 wt%, respectively; the weight percentage, having all the atoms the same mass, corresponds to the ratio between the number of the third-species atoms and the number of all the liquid and gas particles in the system.

Atoms of the rigid walls interact only repulsively with atoms of the third species. This is achieved by truncating the interaction potential (LJ parameters: $\sigma_{3,wall} = 2\sigma$, $\varepsilon_{3,wall} = 2\varepsilon$)
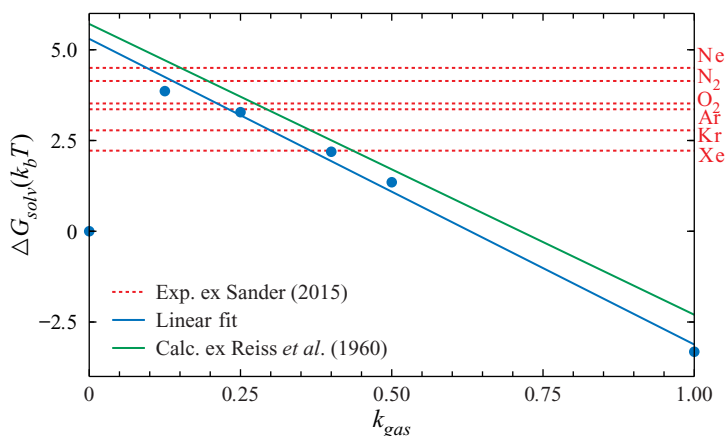
Figure 3. Solvation free energy as a function of the parameter k_{gas} which modulates the interaction between liquid atoms and the dissolved species. Thermodynamic integration results are shown with blue symbols together with a linear fit (blue line), whereas the theory of Reiss *et al.* (1960) is reported in green. For comparison, we also report, in the relevant $k_B T$ units, experimental values of ΔG_{solv} for a selection of gases at 298.15 K; for more information about the experimental data see Sander (2015).

at its minimum ($r_c = 2^{1/6}\sigma_{3,wall}$). The purely repulsive interactions of the rigid walls with the third species have been chosen in order to avoid gas atoms accumulating at the liquid–solid interfaces which is not of interest for our study, since the main purpose of the walls is to apply the shear and control the pressure of the system.

Concerning the interactions within the third species, the LJ size parameters were set equal to the liquid ones, $\sigma_{33} = \sigma$. In order to obtain a gaseous phase, the energy parameter was changed as compared with the value used for liquid species: $\varepsilon_{33} = 0.42\varepsilon$. In all cases, the mass of the third species was set to unity, $m_3 = 1$.

2.2. *Characterization of the gas solubility in the liquids*

In order to characterize solubility of the third species in the two liquids we computed the solvation free energy ΔG_{solv} of the third species by thermodynamic integration. We refer to the supplementary material for details about these simulations. This quantity is related to the solubility of the third species via

$$\Delta G_{solv} = -k_B T \ln(K), \qquad (2.2)$$

where K is the dimensionless Henry constant. Results are shown in figure 3; as expected, higher values of k_{gas} correspond to lower solvation free energies and thus to higher solubilities of the third species. The results obtained via thermodynamic integration are in good agreement with those calculated from the theory of Reiss *et al.* (1960) and Wilhelm & Battino (1971), without fitting – see the supplementary material. The theory is quantitative for intermediate values of k_{gas} but is expected to be less accurate for smaller values; $k_{gas} = 0$ is not considered in the theory.

2.3. *Data analysis*

Velocity and density fields were obtained by dividing the fluid slab into 200 bins along the z-axis and computing averages associated with the corresponding regions of space.
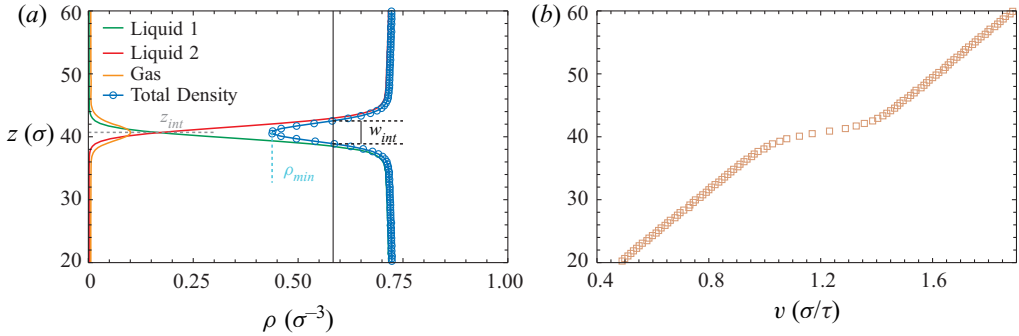
Figure 4. Average density profiles for the two liquid species (green and red lines), for the third species (orange line) and for the total density profiles obtained summing the three profiles (blue line and circles). The definitions of the interface position z_{int} and the density minimum in the interface region ρ_{min}, used to calculate depletion depth δ, are reported. The black line represents the arithmetic average between the bulk density and the minimum density; the intercepts of this line with the total density profile defines the interface width w_{int} (black segment). The cyan dashed line corresponds to the minimum density ρ_{min} reached in the depletion zone of the total density profile. The grey dashed line identifies the z coordinate of the interface z_{int} defined as the point where the two liquids density profiles intersect. The velocity profile (brown squares) is given in (*b*) to show the correspondence between the region w_{int} and the region where the velocity profile deviates from the linear behaviour of the bulk regions.

The slip length L_s was calculated for the liquid–liquid interface at the centre of the computational domain as

$$L_s = \frac{\Delta v}{\dfrac{\partial v}{\partial z}} \tag{2.3}$$

where the velocity jump Δv was computed by fitting the linear velocity fields in the two liquid bulks and subtracting the related velocities calculated at the interface; the shear rate $\partial v/\partial z$ was calculated as the mean of the shear rates in the two bulk regions (figure 2). The location of the interface z_{int} was identified as the coordinate where the two partial density profiles of the liquids cross. This definition of the slip length L_s is equivalent to the one used by Hu *et al.* (2010) and to the classical definition of slip length for solid–liquid slip, in which the slip length L_s is the distance where the extrapolated velocity profile of the upper liquid reaches the velocity of the lower liquid (or solid) at the interface coordinate (figure 2*b*).

The interface properties, i.e. the interface width w_{int} and the depletion depth δ, were computed using the total density profiles (figure 4). Here w_{int} is defined as the distance between the point at which the total density falls below the arithmetic average of the minimum density reached in the depletion region and the bulk value on the liquid 1 side and the point in which the total density raises above the average on the liquid 2 side. The depletion depth, δ, is instead quantified as the difference between the total bulk density and the minimum total density in the interface region.

3. Results and discussion

3.1. *Slip in the presence of gas*

We start our presentation of the results discussing the main quantity characterizing slip at liquid–liquid interfaces, i.e. the slip length L_s. Before a third species is added, the slip
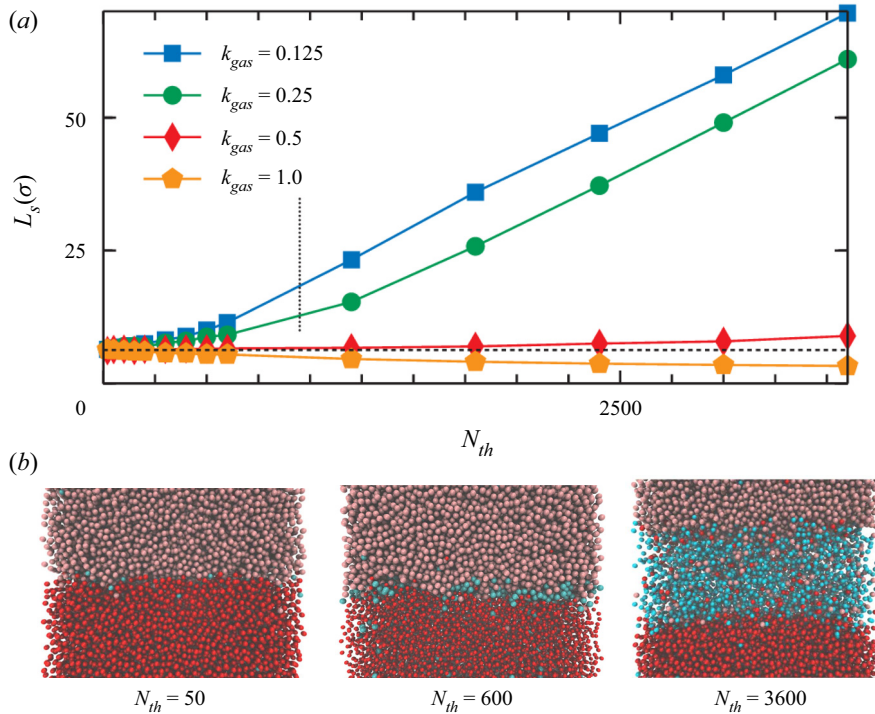
Figure 5. (*a*) Slip length as a function of the number N_{th} of third species atoms for the four values of k_{gas}: 0.125 (blue); 0.25 (green); 0.5 (red); 1.0 (orange). The dashed line represents the value of the slip length without third species, while the dotted vertical line is placed in the region where the transition from dissolved gas to a full gas layer takes place for $k_{gas} = 0.125$ and 0.25. (*b*) Snapshots of systems with $k_{gas} = 0.125$ at different gas concentrations in the vicinity of the interface.

length is of molecular extent, in agreement with previous reports (Padilla *et al.* 1995; Buhn *et al.* 2004; Galliero 2010), $L_s = 6\sigma$, which corresponds to around 2 nm when using the typical characteristic length of water, $\sigma = 0.31$ nm (Abascal & Vega 2005). In figure 5, we analyse the effect of atoms of a third species on slip; the slip length is seen to substantially increase or to decrease depending on the strength of the interactions of the liquid with the third phase. Elucidating this process, along with a discussion on the implications of such behaviour for real world microfluidic flows, is the main focus of the present work.

Figure 5(*a*) shows that the more soluble gases, $k_{gas} = 0.5$ and $k_{gas} = 1.0$, have a minor effect on the slip properties of the system, causing small changes ($k_{gas} = 0.5$) or even a decrease of L_s up to 50 % of the starting slip length ($k_{gas} = 1.0$). Typical velocity fields and density profiles of these systems are shown in figures 2 and 4. The main effect on slip seems to be due to the density depletion observed at the liquid–liquid interface ensuing from the poor miscibility of the two liquids. In these two cases, the third species accumulates at the interface (and in the bulk, see figure 6) without significantly altering its structure. Over the broad range of concentrations explored, only slight changes in the distribution of the third species were observed. This regime thus consists of a gas-enriched liquid–liquid interface, whose properties are analysed in detail in § 3.2.

In the less soluble cases ($k_{gas} = 0.125$ and 0.25), as the number of third species atoms N_{th} increases, the slip length increases as well (figure 5*a*). However, for these two cases, the extent of changes is much larger than for the more soluble gases and more complex slip
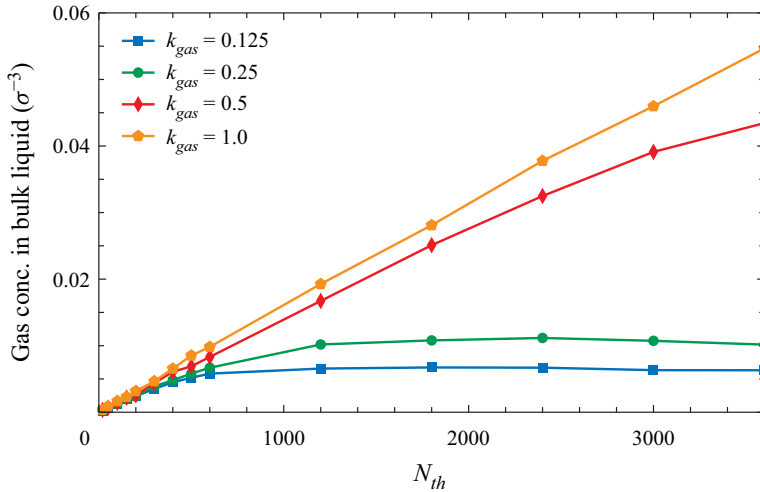
938 A35-9

Figure 6. Plot of the gas concentration in the bulk region of liquid 1 for the four values of k_{gas}: 0.125 (blue); 0.25 (green); 0.5 (red); 1.0 (orange) measured as number of gas atoms per unit volume versus the number N_{th} of third species atoms.

mechanisms emerge. Figure 5(*a*) clearly shows two different regimes for the slip length: one at low concentrations, below $N_{th} \approx 1200$, where the increase in the slip length are moderate and the velocity and density profiles resemble the ones of systems $k_{gas} = 0.5$ and $k_{gas} = 1.0$ (figures 2 and 4); the other regime starts above $N_{th} \approx 1200$ and is characterized by more consistent changes in the slip length, following a linear trend in N_{th} with similar slopes for both cases. The density and velocity profiles are significantly different than in the other cases (figure 8) and show the formation of an independent gas layer interposed between the two liquids (see also figure 5*b*). In this regime, slip is dictated by the (low) viscosity of the gas layer; this mechanism is analysed in detail in § 3.3.

3.2. *Intrinsic slip: gas-enriched interface*

A first regime can be observed for $k_{gas} = 0.5$ and $k_{gas} = 1.0$ at all gas concentrations, and for $k_{gas} = 0.125$ and $k_{gas} = 0.25$ when N_{th} is below a threshold, which, for the current system is $N_{th} \approx 1200$. In this first regime, the gas is observed to progressively accumulate mainly at the liquid–liquid interface filling the depletion region (figure 4). Importantly, the third species shows no particular structure.

The typical velocity profile under shear for these systems is shown in figure 2. The observed behaviour is qualitatively similar to the velocity fields reported by Padilla *et al.* (1995), Galliero (2010) and Poesio, Damone & Matar (2017) for systems without gas. Two linear regions can be observed in the profiles of streamwise velocity, corresponding to the liquid bulks. An abrupt change in the slope is seen at the liquid–liquid interface, which confirms the presence of some degree of slip between the two liquids. Slip can be quantified in terms of the slip length L_s with the usual construction in figure 2. This slip is an 'intrinsic' one, since it is related to molecular interactions occurring across the liquid–liquid interface. Importantly, the measurable effect of the third phase is an indirect one, in that it modifies the interface width w_{int} and its depletion δ, see below.

The physical properties w_{int} and δ characterizing the interface are reported in figure 7 for the gas-enriched interfaces. The plots clearly show that the gas-enrichment of the interface
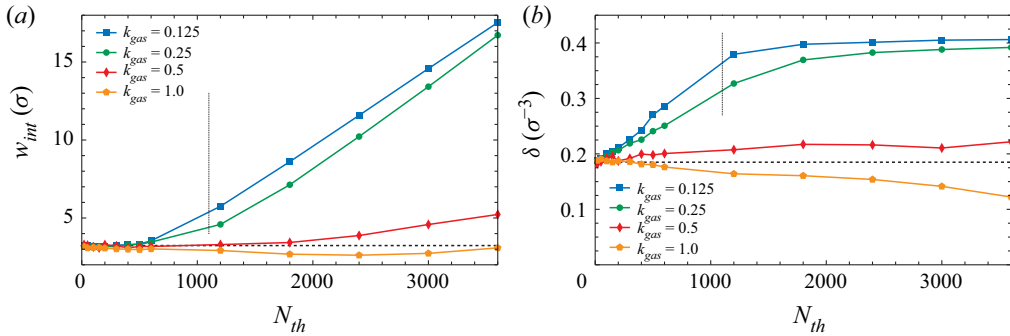
Figure 7. Interfacial width w_{int} (a) and depletion depth δ (b) plotted against the number N_{th} of third species atoms for the four values of k_{gas}: 0.125 (blue); 0.25 (green); 0.5 (red); 1.0 (orange). Error bars are comparable to the point size. Dashed lines represent the values of w_{int} and δ for the system without third species, dotted vertical line are placed where the transition from dissolved gas to a full gas layer takes place for k_{gas} 0.125 and 0.25.

has different effects on its properties depending on the gas–liquid interactions; in turn, these changes are reflected in different trends of the slip length versus N_{th}.

It is important to remark that, for $k_{gas} = 1.0$ and 0.5 the third species can accumulate both in the bulk and at the interface, see figure 6. The local concentration is typically higher at the interface where the density depletion leaves room for the gas; only in the more soluble case $k_{gas} = 1.0$ the concentration of gas dissolved in the liquid bulks is comparable to the concentration in the interface region. However, the competition with the bulk is such that the interface is quickly saturated for these cases, which is reflected in marginal changes of the interface properties.

For $k_{gas} = 1.0$, the interface, i.e. the depletion region, tends to slightly shrink and be replenished, i.e. w_{int} and δ decrease as more atoms of the third species are inserted into the system. This corresponds to a decrease of L_s with N_{th}, due to an improved momentum transfer at the interface: the gas (marginally) improves the coupling between the two liquids.

For $k_{gas} = 0.5$, where no substantial changes in the slip length are observed, w_{int} and δ correspondingly show no considerable changes. On the other hand, in the case of poorly soluble gases ($k_{gas} = 0.125$ and $k_{gas} = 0.25$), the depletion region properties show opposite trends as compared with the case $k_{gas} = 1.0$, getting (marginally) wider and more depleted as more gas is inserted. The combination of these two effects decreases the momentum transfer at the interfaces and is reflected in significant increases of the slip length, which can reach up to around 20σ. In summary, in the intrinsic slip regime we observe a dependence of L_s on the depletion of the interface region, as quantified by w_{int} and δ. We remark that depletion is a static, structural property which depends on the microscopic interactions between species and is independent of the velocity, see § 5 of the supplementary material. An increase in δ and w_{int}, i.e. a thicker and emptier depletion region, causes an increase in the slip length L_s, on the contrary, when the depletion region shrinks and replenishes, L_s decreases.

3.3. *Apparent slip: interposed gas layer*

A distinct regime was observed for low solubilities ($k_{gas} = 0.125$ and $k_{gas} = 0.25$) at relatively high concentrations of the third species ($N_{th} > 1200$). In this regime, we
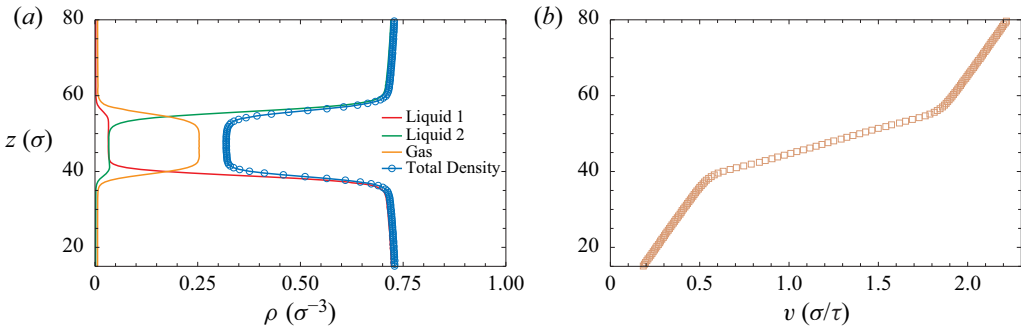
Figure 8. Density (*a*) and velocity profiles (*b*) in the region close to the interfaces for $k_{gas} = 0.125$ and $N_{th} = 3600$. The profiles show the formation of a third phase between the two liquids characterized by a lower density as compared with the two liquid phases. The velocity profile does not exhibit anymore an abrupt change but three approximately linear regions.

observed the formation of an independent layer rich in the third species taking the place of the original liquid–liquid interface, see figure 8. The density of this layer is lower than that of the liquids and its structure is that of a gas. In particular, independent equilibrium simulations at identical temperature, pressure and compositions (see the supplementary material, figure S11) show that the density and the radial distribution functions correspond to those of a bulk gas, allowing us to confirm that the interposed layer consists indeed of a bulk-like 'gas phase'.

The density profiles in the gas-layer regime (figure 8*a*) reveal significant differences as compared with the enriched interface case. The original liquid–liquid interface gets gradually substituted by a well-defined slab of a new lower-density phase mainly constituted by third species atoms and saturated with the two original liquids in solution. With the increase in N_{th} in the system, the thickness of the gas layer increases, as shown by the linear growth of w_{int}, while the concentration of gas dissolved in the original liquid phases remains constant at saturation levels (figure 6). On the other hand, the depletion δ remains constant since the density minimum is reached in correspondence of the new phase, which settles at its bulk value.

The velocity profiles in figure 8(*b*) show that the velocity gradient increases in the interposed layer, due to the lower viscosity of the gas as compared with that of the liquids. The net effect of progressively substituting the liquid–liquid interface by a discrete slab of gas phase is thus that of deteriorating momentum transfer between the two liquids. In this scenario, it is possible to compute an apparent slip length, which accounts for the decreased friction at the interface in an effective way. Such a concept is valid at intermediate scales at which the thickness of the gas layer can be neglected.

Already in the presence of a gaseous layer with a thickness of few atomic diameters we observed large effective slip between the two liquids. Slip increases as additional gas is added and enriches the layer. This very large slip is not to be confused with intrinsic slip at the liquid–liquid interface, since, as the velocity profile shows, there is no abrupt change in the velocity field, but an apparent slip mediated by the low viscosity gaseous layer interposed between the two liquids, see figure 8.

Figure 9(*a*) shows that the slip length in the gas-layer regime increases linearly with the width of the gaseous slab and thus with N_{th}. Furthermore, it can be noticed how the proportionality between L_s and N_{th} is the same for various values of the gas–liquid interactions, as shown by the two curves for $k_{gas} = 0.125$ and $k_{gas} = 0.25$ having the
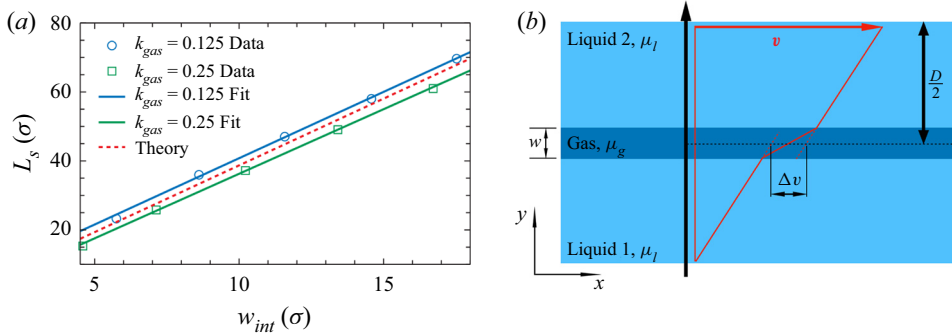
938 A35-12

Figure 9. (*a*) Data for $k_{gas} = 0.125$ (blue circles) and $k_{gas} = 0.25$ (green squares) of the apparent slip length as function of the interface width w_{int} for the systems where the gas layer is fully formed. The blue and green lines are a linear fit to the data, giving as result a theoretical value of the viscosity ratio $\gamma = 4.84$ for $k_{gas} = 0.125$, and $\gamma = 4.74$ for $k_{gas} = 0.25$. The red dotted line has slope $\gamma = 4.87$, calculated using the viscosities obtained via Green–Kubo formalism. (*b*) Sketch of the three-fluids model used to find analytically a relation between the interposed layer thickness and the slip length. The velocity jump is defined in analogy with the one represented in figure 2.

same slope. This finding further confirms that the interposed layer indeed reaches bulk properties which depend almost solely on the gas properties and not on its interactions with the liquid. The only dependence on k_{gas} is indirect and concerns the creation of the layer, which only occurs for gases whose solubility is sufficiently low to allow the gas concentration in the liquid bulk to quickly reach saturation.

Employing the framework introduced in § 1.1, we compute the apparent slip length L_s introduced by an intervening gas layer of given viscosity. At variance with figure 1, we solve for a triphase Couette flow in which the two liquids are symmetric and a gas layer is interposed between them, see figure 9(*b*). We refer the reader to the supplementary material for the full derivation. The main result is that $L_s = (\gamma - 1)\,w$, with $\gamma = \mu_l/\mu_g$ and w the thickness of the gas layer.

The red dashed line in figure 9(*a*) shows a quantitative accord of the slope predicted by the macroscopic Couette model with the numerical simulations. Importantly, we found that the ratio of liquid and gas phase viscosity as deduced from a linear fit of the measured velocity profiles is consistent with independent estimates of γ via the viscosities of the various phases obtained in equilibrium simulations via the Green–Kubo formalism (see the supplementary material for more information).

We further note that, in the gas-layer regime, two independent gas–liquid interfaces form. For both of them the velocity profile is smooth (figure 8*b*) and does not show the distinctive jump of the liquid–liquid interface, cf. figure 2(*b*). In other terms, the slip connected to gas–liquid interfaces is vanishingly small, which likely originates in the capacity of a dense, unstructured, and partially soluble fluid – a gas – to adhere to a liquid interface: the total density profile indeed shows a smooth change between the liquid and gas bulk values (figure 8*a*) without the depletion characterizing the interface between two poorly miscible structured fluids (figure 4). Therefore, one cannot introduce additional slip lengths connected to the two gas–liquid interfaces. We remark that this result is obtained in a rather different regime than previous studies on rarefied gases at solid surfaces (de Gennes 2002; Ramisetti *et al.* 2017). Nonetheless, the vertical offset between the two straight lines at $k_{gas} = 0.125$ and $k_{gas} = 0.25$ in figure 9 seems to suggest a minor role of the gas–liquid interactions on the overall slip length.

3.4. *Intrinsic and apparent slip at LISs*

At LISs, the total slip length is given by the sum of the slip due to the lubricant layer $L_{s,ow}$ and that of the liquid–liquid interface $L_{s,int}$, see (1.2). The present result shows that $L_{s,int}$ can have two different origins: intrinsic, when it emerges from the structure of the liquid–liquid interface, in this case, enriched by a gas phase; or apparent, when a discrete gas layer forms between the two liquids. Only in the case of the gas layer, the contribution of $L_{s,int}$ to (1.2) is significant, up to tens of nanometres. Such values may at least partially explain the large slip lengths reported in recent experiments (Scarratt *et al.* 2020). In the light of the present results, further experiments controlling the gas content are needed in order to assess the relevance of such mechanism in conditions of technological relevance.

Interestingly, we do not observe any breakdown mechanism of the gas layer even at the highest considered gas content, nor its stability is influenced by the shear or the pressure, see the supplementary material. In addition, density profiles like that in figure 8(*a*) show that the gas layer has reached bulk-like characteristics. Together, these two considerations suggest that, under some circumstances, thick gas layers may form at LIS accounting for very large slip. In particular, it is required that the gas has poor solubility and no means to escape in the environment, such that it is forced to accumulate at the liquid–liquid interface. This might be the case for closed systems, such as microfluidic chips, where gas-induced slip lengths of tens of nanometres, such as those computed here, may be important both for interpreting available experiments and to decrease friction at LIS.

One is further tempted to speculate that gas layers similar to those reported here may also form at liquid–solid interfaces, potentially leading to significant slip (de Gennes 2002). Gas accumulation is indeed known to occur for hydrophobic substrates (Tortora *et al.* 2020), leading to the formation of surface nanobubbles (Lohse & Zhang 2015); however, further investigation is needed in order to assess the role of the nanobubble shape and pinning on slip. Indeed, it has been reported that protruding nanobubbles may actually decrease slip or even increase friction (Maali & Bhushan 2013).

4. Conclusions

Non-equilibrium molecular dynamics simulations have been instrumental to provide microscopic insights into slip at liquid–liquid interfaces in the presence of a third species. Dissolved gases are ubiquitous in real world and experimental applications, and are found to significantly alter the microscopic structure of interfaces, resulting in macroscopically observable effects on the flow. More fundamentally, a rich phenomenology is reported for enriched liquid–liquid interfaces, which should be taken into account when considering the boundary condition between two liquids in microscale and nanoscale flows.

In this work, the effect of dissolving a third species on the slip properties was found to depend on the solubility of the enriching species and on the gas content of the system. At low concentrations, the third species tends to accumulate at the liquid–liquid interface altering the local density, thus regulating its intrinsic slip length: poorly soluble species tend to deplete it, thereby effectively reducing the viscous coupling between the two liquids. On the other hand, addition of soluble species replenishes the liquid–liquid interface, increasing the viscous coupling between the liquids.

As the total content of the third species is increased above a critical value, the less soluble species quickly reach saturation in the liquid bulks, leading to the formation of an independent, low-density gas layer interposed between the two liquids. This second regime is associated with large apparent slip lengths scaling linearly with the thickness of the gaseous slab and with the liquid-to-gas viscosity ratio as quantitatively explained by a

three-fluids model. A thickness of the gas layer just above 10 molecular radii (∼3 nm for water) was observed to yield apparent slips exceeding the original liquid–liquid values by roughly one order of magnitude.

The present results reveal a rich phenomenology of relevance for all liquid–liquid interfaces. Of particular interest are LIS for which large slip lengths have been reported (Solomon *et al.* 2014; Scarratt *et al.* 2020), but whose origin is largely unknown. Present simulations suggest that, whereas the intrinsic liquid–liquid slip, even at enriched interfaces, is always very small and comparable to the liquid particle size, the potential build-up of discrete gas layers of nanometre width may contribute to the giant slip lengths measured at LIS. Further studies are needed to verify the presence of such a gas layer in actual experimental conditions and the means to control its thickness. This knowledge will provide an effective and robust means to achieve large slip at LIS to be used, e.g. in drag reduction applications.

Author ORCIDs.
Ⓓ Antonio Tinti https://orcid.org/0000-0002-6750-6503;
Ⓓ Alberto Giacomello https://orcid.org/0000-0003-2735-6982.

Author contributions. A.G. and A.T. designed research. E.T. performed the simulation; A.G., A.T., and E.T. analysed data and wrote the manuscript.

REFERENCES

ABASCAL, J.L.F. & VEGA, C. 2005 A general purpose model for the condensed phases of water: TIP4P/2005. *J. Chem. Phys.* **123**, 234505.

ASMOLOV, E.S, NIZKAYA, T.V. & VINOGRADOVA, O.I. 2018 Enhanced slip properties of lubricant-infused grooves. *Phys. Rev. E* **98**, 033103.

BARRAT, J.L. & CHIARUTTINI, F. 2003 Kapitza resistance at the liquid-solid interface. *Mol. Phys.* **101**, 1605–1610.

BARSKY, S. & ROBBINS, M.O. 2001 Molecular dynamics study of slip at the interface between immiscible polymers. *Phys. Rev. E* **63**, 021801.

BOCQUET, L. & CHARLAIX, E. 2009 Nanofluidics, form bulk to interfaces. *Chem. Soc. Rev.* **39**, 1073–1095.

BOLOGNESI, G., COTTIN-BIZONNE, C. & PIRAT, C. 2014 Evidence of slippage breakdown for a superhydrophobic microchannel. *Phys. Fluids* **26**, 082004.

BROCHARD, F. & DE GENNES, P.G. 1992 Shear-dependent slippage at a polymer/solid interface. *Langmuir* **8** (12), 3033–3037.

BUHN, J.B., BOPP, P.A. & HAMPE, J.M. 2004 A molecular dynamics study of a liquid-liquid interface: structure and dynamics. *Fluid Phase Equilib.* **224**, 221–230.

CAMISASCA, G., TINTI, A. & GIACOMELLO, A. 2020 Gas-induced drying of nanopores. *J. Phys. Chem. Lett.* **7**, 9171.

CARTAGENA, E.J.G., ARENAS, I., BERNARDINI, M. & LEONARDI, S. 2018 Dependence of the drag over super hydrophobic and liquid infused surfaces on the textured surface and Weber number. *Flow Turbul. Combust.* **100**, 945–960.

CHARRAULT, E., LEE, T., EASTON, C.D. & NETO, C. 2016 Boundary flow on end-grafted PEG brushes. *Soft Matt.* **12** (6), 1906–1914.

CHINAPPI, M. & CASCIOLA, C.M. 2010 Intrinsic slip on hydrophobic self-assembled monolayer coatings. *Phys. Fluids* **22** (4), 042003.

CHOI, C.H. & KIM, C.J. 2006 Large slip of aqueous liquid flow over a nanoengineered superhydrophobic surface. *Phys. Rev. Lett.* **96**, 066001.

COSTANTINI, R., MOLLICONE, J.P. & BATTISTA, F. 2018 Drag reduction induced by superhydrophobic surfaces in turbulent pipe flow. *Phys. Fluids* **30**, 025102.

COTTIN-BIZONNE, C., BARRAT, J.L., BOCQUET, L. & CHARLAIX, E. 2003 Low-friction flows of liquid at nanopatterned interfaces. *Nat. Mater.* **2**, 237–240.

COTTIN-BIZONNE, C., CROSS, B., STEINBERGER, A. & CHARLAIX, E. 2005 Boundary slip on smooth hydrophobic surfaces: intrinsic effects and possible artifacts. *Phys. Rev. Lett.* **94**, 056102.

DANIELLO, R.J., WATERHOUSE, N.E. & ROTHSTEIN, J.P. 2009 Drag reduction in turbulent flows over superhydrophobic surfaces. *Phys. Fluids* **21**, 085103.

EHLINGER, Q., JOLY, L. & PIERRE-LOUIS, O. 2013 Giant slip at liquid-liquid interfaces using hydrophobic ball bearings. *Phys. Rev. Lett.* **110**, 104504.

FU, M.K., ARENAS, I., LEONARDI, S. & HULTMARK, M. 2017 Liquid-infused surfaces as a passive method of turbulent drag reduction. *J. Fluid Mech.* **824**, 688–700.

GALLIERO, G. 2010 Lennard–Jones fluid-fluid interfaces under shear. *Phys. Rev. E* **81**, 056306.

DE GENNES, P.G. 2002 On fluid/wall slippage. *Langmuir* **18**, 3413–3414.

GENTILI, D., CHINAPPI, M., BOLOGNESI, G., GIACOMELLO, A. & CASCIOLA, C.M. 2013 Water slippage on hydrophobic nanostructured surfaces: molecular dynamics results for different filling levels. *Meccanica* **48**, 1853–1861.

GENTILI, D., BOLOGNESI, G., GIACOMELLO, A., CHINAPPI, M. & CASCIOLA, C. 2014 Pressure effects on water slippage over silane-coated rough surfaces: pillars and holes. *Microfluid Nanofluid* **16**, 1009–1018.

GIACOMELLO, A., SCHIMMELE, L., DIETRICH, S. & TASINKEVYCH, M. 2016 Perpetual superhydrophobicity. *Soft Matt.* **12**, 8927–8934.

GIACOMELLO, A., SCHIMMELE, L., DIETRICH, S. & TASINKEVYCH, M. 2019 Recovering superhydrophobicity in nanoscale and macroscale surface textures. *Soft Matt.* **15**, 7462–7471.

GOVEAS, J.L. & FREDRICKSON, G.H. 1998 Apparent slip at a polymer-polymer interface. *Eur. Phys. J. B* **2**, 79–92.

HEMEDA, A.A. & TAFRESHI, H.V. 2016 Liquid-infused surfaces with trapped air (LISTA) for drag force reduction. *Langmuir* **32**, 2955–2962.

HU, Y., ZHANG, X. & WANG, W. 2010 Boundary conditions at the liquid-liquid interface in the presence of surfactants. *Langmuir* **26**, 10693–10702.

KOPLIK, J. & BANAVAR, J.R. 1998 No-slip condition for a mixture of two liquids. *Phys. Rev. Lett.* **80**, 5125.

KOPLIK, J. & BANAVAR, J.R. 2006 Slip, immiscibility, and boundary conditions at the liquid-liquid interface. *Phys. Rev. Lett.* **96**, 044505.

LAFUMA, A. & QUÉRÉ, D. 2011 Slippery pre-suffused surfaces. *Europhys. Lett.* **96**, 56001.

LAUGA, E., BRENNER, M.P. & STONE, H.A. 2007 Microfluidics: the no-slip boundary condition. In *Springer Handbook of Experimental Fluid Mechanics* (ed. C. Tropea, A.L. Yarin & J.F. Foss), Springer Handbooks. Springer.

LOHSE, D. & ZHANG, X. 2015 Surface nanobubbles and nanodroplets. *Rev. Mod. Phys.* **87**, 981.

MAALI, A., PAN, Y., BHUSHAN, B. & CHARLAIX, E. 2012 Hydrodynamic drag-force measurement and slip length on microstructured surfaces. *Phys. Rev. E* **85**, 066310.

MAALI, A. & BHUSHAN, B. 2013 Nanobubbles and their role in slip and drag. *J. Phys.: Condens. Matter* **25** (18), 184003.

MARTYNA, G.J., KLEIN, M.L. & TUCKERMAN, M. 1992 Nosé–Hoover chains: the canonical ensemble via continuous dynamics. *J. Chem. Phys.* **97**, 2635–2643.

MISTURA, G. & PIERNO, M. 2017 Drop mobility on chemically heterogeneous and lubricant-impregnated surfaces. *Adv. Phys.: X* **2**, 591–607.

NAVIER, C.L.M.H. 1823 Mémoire sur les lois du mouvement des fluides. *Mémoires de l'Académie Royale des Sciences de l'Institut de France* **6**, 389–440.

PADILLA, P., TOXVAERD, S. & STECKI, J. 1995 Shear flow at liquid-liquid interfaces. *J. Chem. Phys.* **103**, 716.

PEAUDECERF, F.J., LANDEL, J.R., GOLDSTEIN, R.E. & LUZZATTO-FEGIZ, P. 2017 Traces of surfactants can severely limit the drag reduction of superhydrophobic surfaces. *Proc. Natl Acad. Sci. USA* **114**, 7254–7259.

PLIMPTON, S. 1995 Fast parallel algorithms for short-range molecular dynamics. *J. Comput. Phys.* **117**, 1–19.

POESIO, P., DAMONE, A. & MATAR, O.K. 2017 Slip at liquid-liquid interfaces. *Phys. Rev. Fluids* **2**, 044004.

RAMISETTI, S.B., BORG, M.K., LOCKERBY, D.A. & REESE, J.M. 2017 Liquid slip over gas nanofilms. *Phys. Rev. Fluids* **2**, 084003.

REISS, H., FRISCH, H.L., HELFAND, E. & LEBOWITZ, J.L. 1960 Aspects of the statistical thermodynamics of real fluids. *J. Chem. Phys.* **32**, 119–124.

ROTHSTEIN, J.P. 2010 Slip on superhydrophobic surfaces. *Annu. Rev. Fluid Mech.* **42**, 89–109.

SANDER, R. 2015 Compilation of Henry's law constants (version 4.0) for water as solvent. *Atmos. Chem. Phys.* **15**, 4399–4981.

SCARRATT, L.R.J., ZHU, L. & NETO, C. 2020 Large effective slip on lubricated surfaces measured with colloidal probe AFM. *Langmuir* **6**, 6033–6040.

SECCHI, E., MARBACH, S., NIGUÈS, A., STEIN, D., SIRIA, A. & BOCQUET, L. 2016 Massive radius-dependent flow slippage in carbon nanotubes. *Nature* **537**, 210–213.

SEMPREBON, C., MCHALE, G. & KUSUMAATMAJA, H. 2017 Apparent contact angle and contact angle hysteresis on liquid infused surfaces. *Soft Matt.* **13**, 101–110.

SMITH, J.D., DHIMAN, R., ANAND, S., REZA-GARDUNO, E., COHEN, R.E., MCKINLEY, G.H. & VARANASI, K.K. 2013 Droplet mobility on lubricant-impregnated surfaces. *Soft Matt.* **9**, 1772–1780.

SOLOMON, B.R., KHALIL, K.S. & VARANASI, K.K. 2014 Drag reduction using lubricant-impregnated surfaces in viscous laminar flow. *Langmuir* **30**, 10970–10976.

TINTI, A., GIACOMELLO, A., GROSU, Y. & CASCIOLA, C.M. 2017 Intrusion and extrusion of water in hydrophobic nanopores. *Proc. Natl Acad. Sci. USA* **114** (48), E10266–E10273.

TINTI, A., GIACOMELLO, A. & CASCIOLA, C.M. 2018 Vapor nucleation paths in lyophobic nanopores. *Eur. Phys. J.* E **41**, 52.

TODD, B.D. & DAIVIS, P.J. 2017 *Nonequilibrium Molecular Dynamics Theory, Algorithms and Applications*. Cambridge University Press.

TORTORA, M., MELONI, S., TAN, B.H., GIACOMELLO, A., OHL, C.D. & CASCIOLA, C.M. 2020 The interplay among gas, liquid and solid interactions determines the stability of surface nanobubbles. *Nanoscale* **12**, 22698–22709.

VINOGRADOVA, O.I. & BELYAEV, A.V. 2011 Wetting, roughness and flow boundary conditions. *J. Phys.: Condens. Matter* **23**, 184104.

WILHELM, E. & BATTINO, R. 1971 Estimation of Lennard–Jones (6, 12) pair potential parameters from gas solubility data. *J. Chem. Phys.* **55**, 4012.

WONG, T., KANG, S.H., TANG, S.K.Y., SMYTHE, E.J., HATTON, B.D., GRINTHAL, A. & AIZENBERG, J. 2011 Bioinspired self-repairing slippery surfaces with pressure-stable omniphobicity. *Nature* **477**, 443–447.

YBERT, C., BARENTIN, C., COTTIN-BIZONNE, C., JOSEPH, P. & BOCQUET, L. 2007 Achieving large slip with superhydrophobic surfaces: scaling laws for generic geometries. *Phys. Fluids* **19**, 123601.